Research Square

Preprints are preliminary reports that have not undergone peer review.
They should not be considered conclusive, used to inform clinical practice,
or referenced by the media as validated information.

Enhanced Microwave Absorption in $Ba_{0.6}Sr_{0.4}Fe_{12-}ZnO_{19}$ Hexaferrites via Impedance Matching Optimization for X-Band Radar Applications

Maya Puspitasari Izaak
Pelita Harapan University
Henni Sitompul
Pelita Harapan University
Yana Taryana
National Research and Innovation Agency
Nanang Sudrajat
National Research and Innovation Agency
Jan Setiawan
National Research and Innovation Agency
Yunasfi Yunasfi
National Research and Innovation Agency
Mashadi Mashadi
National Research and Innovation Agency
Didin S Winatapura
National Research and Innovation Agency
Wisnu Ari Adi
National Research and Innovation Agency
Tesalonika Siregar
University of Indonesia
Yohanes Edi Gunanto
Pelita Harapan University
Dianta Ginting
dianta.ginting@mercubuana.ac.id
Mercu Buana University

correspondence

Keywords: Hexaferrite, Zinc substitution, Microwave absorber, C–X band, Impedance matching

Posted Date: March 2nd, 2026

DOI: https://doi.org/10.21203/rs.3.rs-8875692/v1

License: This work is licensed under a Creative Commons Attribution 4.0 International License.
Read Full License

Additional Declarations: No competing interests reported.

Version of Record: A version of this preprint was published at Journal of Materials Science: Materials in Electronics on July 7th, 2026. See the published version at https://doi.org/10.1007/s10854-026-17900-x.

Abstract

Achieving optimal microwave absorption performance in ferrite-based materials requires a delicate balance between magnetic loss, dielectric loss, and impedance matching rather than maximizing magnetic properties alone. In this work, Zn^{2+}-substituted $Ba_{0.6}Sr_{0.4}Fe_{12-x}Zn_xO_{19}$ (x = 0.25, 0.50, and 0.75) M-type hexaferrites were synthesized via a conventional solid-state reaction method, and their structural, magnetic, and electromagnetic absorption properties were systematically investigated. X-ray diffraction analysis confirmed hexagonal M-type phase formation, while scanning electron microscopy revealed composition-dependent grain growth from 200–300 nm (x = 0.25) to 3.1–4.3 μm (x = 0.75). Magnetic measurements showed that saturation magnetization decreased from 57.95 emu/g (x = 0.25) to 37.29 emu/g (x = 0.50) due to weakened superexchange interactions. Despite this reduction in magnetic strength, the x = 0.50 composition exhibited superior microwave absorption performance, achieving a minimum reflection loss of − 24.94 dB at 10.78 GHz, corresponding to 99.7% absorption efficiency. Effective absorption (RL < − 10 dB) was maintained across the C–X band (4–12 GHz), with the strongest attenuation occurring in the X-band region (8–12 GHz). Electromagnetic analysis revealed that the enhanced absorption originates from optimized impedance matching ($Z_i/Z_0 \approx 1$) and synergistic magnetic–dielectric loss mechanisms, including natural ferromagnetic resonance and interfacial polarization. These findings demonstrate that impedance matching optimization, rather than high saturation magnetization, governs the microwave absorption efficiency in Zn-substituted Ba–Sr hexaferrites, providing practical design guidelines for X-band radar absorbing materials.

1. Introduction

Microwave absorbing materials (MAMs) play a crucial role in electromagnetic interference (EMI) mitigation, radar stealth technology, and high-frequency communication systems. In recent years, increasing attention has been directed toward magnetic ceramics owing to their intrinsic magnetic loss mechanisms and excellent thermal and chemical stability at gigahertz frequencies [1–4]. In parallel, recent advances in low-dimensional and hybrid absorber systems have highlighted the importance of microstructural and compositional engineering to achieve optimal impedance matching and broadband absorption performance [5]. Among various magnetic ceramic candidates, hexaferrites remain particularly attractive because their magnetocrystalline anisotropy enables natural ferromagnetic resonance in the microwave regime, making them promising candidates for radar-frequency absorbers [6–8].

M-type barium hexaferrite ($BaFe_{12}O_{19}$) crystallizes in a magnetoplumbite-type hexagonal structure, where the complex cationic distribution over five distinct crystallographic sites governs its magnetic anisotropy and resonance behavior [9]. Partial substitution of Ba^{2+} with Sr^{2+} has been reported to modify lattice parameters and enhance magnetic stability without severely degrading magnetization, thereby improving high-frequency magnetic response [10, 11]. Concurrently, substitution at the Fe^{3+} sites with non-magnetic or weakly magnetic cations such as Zn^{2+} has emerged as an effective strategy to tailor magnetic anisotropy, weaken superexchange interactions, and promote dielectric polarization [12–15].

Recent studies have demonstrated that Zn-substituted hexaferrites can exhibit enhanced microwave absorption performance when an appropriate balance between magnetic loss, dielectric loss, and impedance matching is achieved [15–18]. This dual-substitution approach offers unique opportunities to decouple magnetic and dielectric contributions, enabling independent optimization of electromagnetic parameters for specific frequency bands.

However, most previous works focus either on single-cation substitution or broadband absorption behavior, while systematic investigations addressing the interplay between Zn-induced magnetic softening, microstructural evolution, and impedance matching in Ba–Sr co-substituted hexaferrites remain limited, particularly in the technologically important X-band (8–12 GHz) [19]. More critically, conventional design strategies often emphasize maximizing saturation magnetization to enhance magnetic loss, overlooking the fundamental requirement that efficient microwave absorption depends not solely on loss magnitude but on achieving optimal impedance matching ($Z_i/Z_0 \approx 1$) to minimize surface reflection and maximize wave penetration into the absorber. This traditional magnetization-dominant paradigm frequently results in suboptimal absorption performance despite high magnetic loss, as impedance mismatch prevents effective electromagnetic wave entry into the material.

In this work, $Ba_{0.6}Sr_{0.4}Fe_{12-x}Zn_xO_{19}$ (x = 0.25, 0.50, and 0.75) hexaferrites were synthesized via a conventional solid-state reaction method to systematically investigate the composition-dependent interplay between structural evolution, magnetic properties, and microwave absorption mechanisms. The effects of Zn substitution on phase evolution, grain growth, magnetic parameters, and electromagnetic response were comprehensively analyzed through X-ray diffraction (XRD), scanning electron microscopy (SEM), vibrating sample magnetometry (VSM), and vector network analyzer (VNA) measurements. By correlating magnetic parameters with complex permittivity, permeability, and reflection loss behavior, this study aims to clarify the dominant absorption mechanisms and establish composition-dependent design rules for high-performance X-band microwave absorbers. Particular emphasis is placed on the X-band region (8–12 GHz), which is of significant technological interest for high-resolution radar systems, satellite communications, and stealth applications, while also evaluating performance across the broader C–X band (4–12 GHz) to assess versatility for long-range surveillance applications.

Unlike conventional approaches that emphasize high saturation magnetization as the primary design criterion, this study demonstrates that optimal microwave absorption performance is governed by impedance matching optimization and balanced magnetic–dielectric synergy rather than magnetic loss magnitude alone. Notably, the composition with x = 0.50 exhibits superior reflection loss (− 24.94 dB at 10.78 GHz, corresponding to 99.7% absorption efficiency) despite exhibiting reduced saturation magnetization compared to lightly substituted samples, highlighting the decisive role of impedance matching induced by controlled Zn substitution and phase heterogeneity. Electromagnetic analysis reveals that the enhanced absorption originates from the synergistic combination of optimized impedance matching ($Z_i/Z_0 \approx 1$), natural ferromagnetic resonance, and interfacial polarization effects. This work provides quantitative experimental evidence that challenges the traditional magnetization-

dominant paradigm and offers practical design guidelines for tailoring ferrite-based absorbers for X-band radar-frequency applications through impedance engineering rather than magnetic loss maximization.

2. Materials and Methods

2.1. Raw Materials and Chemicals

The raw materials used in this study were classified into two categories: (1) high-purity analytical-grade chemicals for fundamental research, and (2) industry-grade precursors sourced locally and internationally. For the development of a laboratory-scale prototype under the basic research framework, analytical-grade chemicals were employed to ensure high reproducibility and phase purity.

The chemical precursors used include barium carbonate ($BaCO_3$), strontium carbonate ($SrCO_3$), iron(III) oxide (Fe_2O_3), zinc oxide (ZnO), and titanium dioxide (TiO_2), all of which were obtained from Merck and/or Sigma-Aldrich with pro analysis (p.a.) grade purity. Ethanol was also used as a dispersing agent during the mixing process.

2.2. Synthesis via Solid-State Reaction

The $Ba_{0.6}Sr_{0.4}Fe_{12-}$□Zn□O_{19} (x = 0.25, 0.50, 0.75) samples were synthesized through the conventional solid-state reaction method. The stoichiometric amounts of $BaCO_3$, $SrCO_3$, Fe_2O_3, and ZnO were weighed and mixed thoroughly in ethanol using a ball mill to ensure homogeneous distribution of the precursors. The resulting slurry was dried, ground into fine powder, and subjected to calcination at a temperature of 1000°C for several hours to initiate phase formation. The calcined powders were then compacted into pellets using a uniaxial press and sintered at high temperatures (1000°C) in air to promote crystallization and densification. The $Ba_{0.6}Sr_{0.4}Fe_{12-}$□Zn□O_{19} samples (x = 0.25, 0.50, 0.75) were then named BSF-0.25, BSF-0.50 and BSF-0.75, respectively.

2.3. Characterization Techniques

The phase composition and crystallographic structure of the sintered samples were characterized using X-ray Diffraction (XRD) with Cu Kα radiation (λ = 1.5406 Å). Surface morphology and microstructural features were examined by Scanning Electron Microscopy (SEM). Magnetic properties, including saturation magnetization and coercivity, were measured using a Vibrating Sample Magnetometer (VSM) under an applied magnetic field of up to ± 15 kOe. The microwave absorption performance was evaluated using a Vector Network Analyzer (VNA) by measuring the reflection loss (RL) in the 4–12 GHz frequency range.

3. Results and Discussion

3.1. Phase structure and crystallography

X-ray diffraction analysis was performed to investigate the phase composition, crystallographic structure, and structural evolution of $Ba_{0.6}Sr_{0.4}Fe_{12-}$ZnO_{19} (x = 0.25, 0.50, 0.75) hexaferrites as a function of Zn substitution. Figure 1(a–c) presents the Rietveld-refined XRD patterns of BSF-0.25, BSF-0.50, and BSF-0.75 samples, respectively, along with a comparative overlay in Fig. 1(d). The diffraction patterns of all three samples exhibit characteristic peaks of the M-type hexaferrite phase with magnetoplumbite-type hexagonal structure (space group $P6_3/mmc$. The most intense reflections are indexed to the (107), (114), (203), (205), (217), (304), and (220) planes, which are typical signatures of the M-type hexagonal ferrite structure.

The BSF-0.25 sample (Fig. 1a) displays sharp, well-defined diffraction peaks with minimal background noise and high peak intensities, indicating excellent crystallinity and nearly single-phase formation. Rietveld refinement shows good agreement between observed (I(obs), blue circles) and calculated (I(calc), red line) patterns, with a relatively flat difference curve (Obs-Calc, yellow line), confirming successful incorporation of Zn^{2+} into the Ba–Sr hexaferrite lattice without significant secondary phase formation. The sharpness of reflections and narrow full-width at half-maximum (FWHM) values suggest superior long-range structural order and large coherent scattering domains, which are favorable for strong ferromagnetic coupling and well-defined magnetic resonance behavior.

In contrast, the BSF-0.50 sample (Fig. 1b) reveals the emergence of weak additional reflections that can be attributed to secondary phases, along with a noticeable reduction in the intensity of main hexaferrite peaks. Careful examination of the diffraction pattern indicates the presence of minor Fe_3O_4 (magnetite, cubic spinel structure) and/or α-Fe_2O_3 (hematite, rhombohedral structure) phases, as evidenced by small peaks appearing at $2\theta \approx 30°$, 35°, and 62°, which do not correspond to the M-type hexaferrite structure. These secondary phases likely originate from partial decomposition or incomplete solid-state reaction at intermediate Zn substitution levels, where the thermodynamic stability of the M-type phase is compromised by disrupted charge balance and altered cation distribution. The formation of Fe_3O_4 and Fe_2O_3 suggests that excess Zn^{2+} may disrupt the charge balance within the hexaferrite structure, leading to the segregation of iron-rich oxide phases during high-temperature sintering. The reduced peak intensities and increased FWHM values compared to BSF-0.25 further indicate decreased crystallinity and the presence of structural heterogeneity. Despite the presence of secondary phases, the M-type hexaferrite remains the dominant phase, with characteristic peaks retaining significant intensity. The more pronounced discrepancies in the difference curve (Obs-Calc), particularly in the 2θ range of 30–40°, reflect the multiphase nature of this composition and suggest that the single-phase structural model used for refinement does not fully capture the complexity of the observed diffraction data.

Interestingly, the BSF-0.75 sample (Fig. 1c) exhibits a return to predominantly single-phase behavior, with secondary phase reflections becoming less prominent compared to BSF-0.50. However, subtle peak broadening and slight asymmetry are observed, particularly for high-angle reflections such as (220), (2,0,14), and (317), indicating increased microstrain and/or reduced crystallite size induced by higher Zn incorporation. The absence of clearly resolved secondary phase peaks in BSF-0.75, despite the higher Zn content, suggests that at this composition, Zn^{2+} ions are more effectively accommodated within the

hexaferrite lattice, possibly through partial occupancy of octahedral (12k, $4f_2$, 2a) and tetrahedral ($4f_1$) sites, leading to anisotropic lattice distortion rather than phase segregation. The peak intensities recover to intermediate levels between BSF-0.25 and BSF-0.50, while the broadening of high-angle reflections implies that Zn substitution preferentially affects certain crystallographic directions, introducing structural disorder without completely destabilizing the M-type framework. The difference curve shows moderate oscillations, indicating reasonable refinement quality despite the presence of lattice strain.

The overlay comparison in Fig. 1(d) reveals systematic compositional trends across the three samples. Close inspection of the main (114) and (107) reflections shows a gradual shift toward lower 2θ angles as x increases from 0.25 to 0.75, indicating progressive expansion of the hexagonal unit cell. This shift is consistent with the replacement of smaller Fe^{3+} ions (ionic radius: 0.645 Å for octahedral coordination) with larger Zn^{2+} ions (ionic radius: 0.74 Å), which increases the average cation radius and expands interatomic distances. The lattice expansion is further supported by the systematic decrease in peak intensity and increase in FWHM with increasing Zn content, reflecting the introduction of lattice strain and local structural disorder due to ionic size mismatch and charge compensation effects. Quantitative Rietveld refinement can provide precise lattice parameters (a and c) and crystallite sizes for each composition, enabling detailed correlation with magnetic and electromagnetic properties.

Scanning electron microscopy (SEM) was employed to investigate the surface morphology and grain size distribution of $Ba_{0.6}Sr_{0.4}Fe_{12-}$□Zn□O_{19} hexaferrites as a function of Zn substitution. Figure 2 presents representative SEM micrographs at 10,000× magnification, revealing distinct compositional dependence of grain morphology and densification behavior. The BSF-0.25 sample (Fig. 2a) exhibits a relatively fine and uniform microstructure with well-defined, equiaxed grains ranging from 200 to 300 nm. Clear grain boundaries and moderate agglomeration are evident, with particles retaining individual identity. In contrast, the BSF-0.50 sample (Fig. 2b) reveals dramatic microstructural coarsening, with irregular, heterogeneous grains ranging from 1.5 to 2.3 μm, representing a 5–8 fold increase in grain size. Pronounced agglomeration, grain coalescence, and neck formation are observed, indicative of enhanced solid-state diffusion and grain boundary migration. The BSF-0.75 sample (Fig. 2c) exhibits further grain growth to 3.1–4.3 μm, with highly irregular polygonal morphologies and extensive coalescence characteristic of exaggerated grain growth through Ostwald ripening mechanisms. The systematic grain size evolution follows an approximately exponential relationship with Zn content, with dimensions increasing by a factor of ~ 15 from BSF-0.25 to BSF-0.75.

The observed grain coarsening behavior can be attributed to the influence of Zn^{2+} substitution on sintering kinetics and grain boundary chemistry. Zinc ions, which preferentially occupy tetrahedral ($4f_1$) sites in the hexaferrite structure, disrupt superexchange interactions between Fe^{3+} ions and reduce the thermodynamic stability of the magnetoplumbite lattice. This destabilization enhances cation mobility and lowers the activation energy for grain boundary migration during high-temperature sintering, leading to accelerated grain growth with increasing Zn content. The heterogeneous grain size distribution and irregular morphology of BSF-0.50 correlate well with the multiphase composition observed in XRD analysis (Fig. 1b), suggesting that the coexistence of M-type hexaferrite, Fe_3O_4, and Fe_2O_3 phases

creates compositional gradients that drive non-uniform grain growth. Additionally, the partial formation of zinc-rich phases may act as sintering aids that promote densification and grain coalescence. These microstructural trends are consistent with previous reports on Zn-substituted hexaferrites [20].

The microstructural characteristics have profound implications for electromagnetic absorption performance. The fine-grained, single-phase microstructure of BSF-0.25, while advantageous for maintaining high magnetization through domain wall pinning, suffers from limited interfacial polarization and potential impedance mismatch. Conversely, the coarse-grained, multiphase microstructure of BSF-0.50 provides an optimal balance between magnetic loss (through natural ferromagnetic resonance) and dielectric loss (through Maxwell-Wagner interfacial polarization at phase boundaries), while simultaneously achieving favorable impedance matching through balanced complex permittivity and permeability. The extreme grain coarsening in BSF-0.75, despite further softening the magnetic response, may compromise absorption efficiency by reducing interfacial area and creating impedance imbalance. These structure–property correlations underscore that intermediate grain sizes (~ 1.5–2.3 μm) and controlled phase heterogeneity are critical for achieving superior impedance matching and microwave absorption, rather than fine grains or high crystallinity alone.

3.3. Magnetic properties and magnetization behavior

Magnetic hysteresis measurements were performed at room temperature using a vibrating sample magnetometer (VSM) under an applied field of ± 1 T to elucidate the effects of Zn substitution on magnetization behavior and magnetic anisotropy. Figure 3 presents the M–H hysteresis loops for all three compositions, while Table 2 summarizes the extracted magnetic parameters, including saturation magnetization (Ms), remanent magnetization (Mr), coercivity (Hc), and squareness ratio (Mr/Ms). The BSF-0.25 sample exhibits the highest saturation magnetization (Ms = 57.95 emu/g) with remanence of Mr = 30.8 emu/g and coercivity of Hc = 346 Oe. The relatively square-shaped hysteresis loop and high Mr/Ms ratio of 0.531 indicate strong uniaxial magnetic anisotropy and well-defined magnetic domain alignment, consistent with the single-phase M-type hexaferrite structure and fine grain size (200–300 nm) observed in XRD and SEM analyses. The high magnetization is attributed to strong Fe^{3+}–O^{2-}–Fe^{3+} superexchange interactions across the magnetoplumbite lattice, which remain largely intact at low Zn substitution levels. The moderate coercivity suggests that the nanoscale grains provide sufficient domain wall pinning to stabilize magnetic anisotropy without excessive hardening.

In stark contrast, the BSF-0.50 sample displays a dramatic reduction in saturation magnetization to Ms = 37.29 emu/g (a 36% decrease relative to BSF-0.25), accompanied by reduced remanence (Mr = 19.0 emu/g) and slightly increased coercivity (Hc = 388 Oe). The narrower hysteresis loop and lower squareness ratio (Mr/Ms = 0.509) reflect weakened magnetic coupling and increased magnetic softening. This behavior directly correlates with the multiphase composition revealed by XRD (Fig. 1b), where the coexistence of M-type hexaferrite with weakly magnetic α-Fe_2O_3 (antiferromagnetic or weakly ferromagnetic) and Fe_3O_4 (ferrimagnetic with lower magnetic moment than M-type hexaferrite) dilutes the overall magnetization. The disruption of long-range magnetic ordering by Zn^{2+} substitution at Fe^{3+}

sites further weakens superexchange pathways, reducing exchange coupling between neighboring iron ions. Additionally, the coarse-grained microstructure (1.5–2.3 μm) introduces competing effects: larger grains typically reduce coercivity by facilitating domain wall motion, yet the slightly elevated Hc in BSF-0.50 suggests that the heterogeneous phase boundaries and compositional gradients act as magnetic domain pinning centers, partially compensating for grain coarsening effects. The reduced magnetization, while detrimental to magnetic loss magnitude, plays a critical role in optimizing impedance matching by balancing magnetic and dielectric contributions, as will be discussed in subsequent sections.

Table 1
Magnetic parameters extracted from VSM hysteresis measurements at 300 K under ± 1 T applied field. Mr/Ms ratio indicates magnetic anisotropy and loop squareness. BSF-0.50 exhibits the lowest Ms but highest Hc, correlating with multiphase composition (XRD) and coarse-grained microstructure (SEM).

Sample	M_s (emu/g)	M_r (emu/g)	H_c (Oe)	*Mr/Ms*
BSF-0.25	57.952	30.8	346	0.531
BSF-0.50	37.289	19.0	388	0.509
BSF-0.75	52.212	25.3	327	0.484

Interestingly, the BSF-0.75 sample exhibits partial magnetic recovery, with Ms = 52.21 emu/g, Mr = 25.3 emu/g, and the lowest coercivity (Hc = 327 Oe) among the three compositions. The intermediate hysteresis loop width and squareness ratio (Mr/Ms = 0.484) indicate restored ferromagnetic coupling compared to BSF-0.50, despite higher Zn content. This magnetic recovery can be attributed to two factors: (1) the return to predominantly single-phase M-type structure (as evidenced by reduced secondary phase reflections in XRD, Fig. 1c), which restores superexchange connectivity, and (2) the formation of large, well-crystallized grains (3.1–4.3 μm) that reduce grain boundary scattering and facilitate long-range magnetic ordering within individual grains. However, the lowest Mr/Ms ratio reflects increased magnetic softness, consistent with the reduced domain wall pinning density in coarse-grained systems. The systematic trends in magnetic parameters across the three compositions demonstrate that optimal microwave absorption performance does not require maximum saturation magnetization. Instead, the BSF-0.50 composition, despite exhibiting the lowest Ms, achieves superior reflection loss (−24.94 dB at 10.78 GHz) by leveraging its multiphase microstructure to optimize impedance matching through balanced magnetic–dielectric synergy. This finding challenges the conventional magnetization-dominant design paradigm and underscores the decisive role of impedance engineering in determining microwave absorption efficiency.

3.4. Electromagnetic parameters (ε, μ)

The microwave absorption performance of a material is fundamentally governed by its complex electromagnetic parameters—complex permittivity ($\varepsilon_r = \varepsilon' - j\varepsilon''$) and complex permeability ($\mu_r = \mu' - j\mu''$)—which determine both the energy dissipation mechanisms and impedance matching characteristics. Based on transmission line theory, the reflection loss (RL) can be expressed by Equations (1) and (2) [21]:

$$RL\ (dB) = -20\log\left|\frac{Z_{in} - Z_o}{Z_{in} + Z_o}\right| \quad (1)$$

$$Z_{in} = Z_o\sqrt{\frac{\mu_r}{\epsilon_r}}\tanh\left(j\frac{2\pi fd}{c}\left(\sqrt{\mu_r\epsilon_r}\right)\right) \quad (2)$$

where Z_i is the input impedance of the absorbing material, Z_o is the impedance of free space (377 Ω), ε_r and μ_r are the complex permittivity and permeability, d is the absorber thickness, f is the frequency, and c is the speed of light. Optimal microwave absorption requires not only high electromagnetic loss (large ε" and μ") but also, critically, impedance matching ($Z_i/Z_o \approx 1$) to minimize surface reflection and maximize wave penetration.

Figure 4(a–b) presents the frequency-dependent real and imaginary parts of complex permittivity and permeability for $Ba_{0.6}Sr_{0.4}Fe_{12-x}Zn_xO_{19}$ hexaferrites measured by vector network analyzer (VNA) in the 4–12 GHz range. The real permittivity (ε', solid lines, Fig. 4a) exhibits pronounced dispersion behavior, with values decreasing from approximately 50–60 at 4 GHz to 2–10 at 12 GHz for all samples, characteristic of Debye-type dielectric relaxation. The BSF-0.75 sample displays the highest ε' values (50–25) across the 4–8 GHz range, which can be attributed to enhanced interfacial polarization arising from its coarse-grained microstructure (3.1–4.3 μm, from SEM) that provides extensive grain boundary area for charge accumulation at Maxwell-Wagner interfaces. The BSF-0.50 sample exhibits intermediate ε' values (20–10), while BSF-0.25 shows moderate permittivity (~ 50 at 4 GHz, decreasing to ~ 5 at 12 GHz). The imaginary permittivity (ε", dotted lines) follows similar trends, with BSF-0.50 showing a pronounced peak near 6 GHz, indicative of dipolar relaxation processes associated with heterogeneous phase boundaries (M-type hexaferrite/Fe_3O_4/Fe_2O_3 interfaces observed in XRD, Fig. 1b).

The real permeability (μ', solid lines, Fig. 4b) exhibits more complex frequency dependence compared to permittivity, with values ranging from 5–60 at 4 GHz and generally decreasing toward higher frequencies, though with notable fluctuations reflecting magnetic resonance phenomena. The BSF-0.25 and BSF-0.75 samples display higher μ' values at low frequencies (4–6 GHz), consistent with their higher saturation magnetization (Ms = 57.95 and 52.21 emu/g, respectively, from VSM measurements). In contrast, BSF-0.50 exhibits lower μ' values throughout the frequency range, reflecting its reduced magnetization (Ms = 37.29 emu/g) due to the presence of weakly magnetic secondary phases. However, this reduced

magnetic contribution is compensated by enhanced dielectric loss, as discussed below. The imaginary permeability (μ", dotted lines) reveals multiple resonance features, particularly for BSF-0.25 and BSF-0.75, indicating natural ferromagnetic resonance (FMR) and domain wall resonance contributions to magnetic loss. Notably, the BSF-0.50 sample shows lower μ" values, further confirming weakened magnetic loss mechanisms in this composition.

The energy dissipation characteristics are quantified through dielectric loss tangent (tan $\delta_\varepsilon = \varepsilon''/\varepsilon'$, Fig. 4c) and magnetic loss tangent (tan $\delta_\mu = \mu''/\mu'$, Fig. 4d), which reveal the relative contributions of polarization and magnetic processes to microwave attenuation. The BSF-0.50 sample exhibits exceptionally high dielectric loss across the entire 4–12 GHz range, with tan δ_ε reaching peak values of ~ 3.8 at 9 GHz and ~ 3.3 at 11 GHz in the X-band region. This dominant dielectric loss behavior originates from multiple relaxation mechanisms: (i) interfacial (Maxwell-Wagner) polarization at heterogeneous phase boundaries between M-type hexaferrite, Fe_3O_4, and Fe_2O_3, (ii) dipolar polarization associated with lattice defects and oxygen vacancies induced by Zn substitution, and (iii) ionic polarization from Zn^{2+}/Fe^{3+} disorder at octahedral and tetrahedral sites. The BSF-0.25 and BSF-0.75 samples display moderate dielectric loss (tan δ_ε ~ 0.5–2.5), with BSF-0.75 showing elevated loss at low frequencies (4–8 GHz) due to its coarse-grained microstructure.

In contrast, magnetic loss (Fig. 4d) is dominated by the BSF-0.25 sample, which exhibits sharp resonance peaks at ~ 8 GHz (tan δ_μ ~ 2.9) and ~ 11 GHz (tan δ_μ ~ 3.9), characteristic of natural ferromagnetic resonance (FMR) arising from magnetocrystalline anisotropy in the well-crystallized M-type hexaferrite phase. The resonance frequency of FMR can be estimated by $f_r = \gamma H_a$, where γ is the gyromagnetic ratio and H_a is the anisotropy field, which is maximized in single-phase, fine-grained systems like BSF-0.25. The BSF-0.75 sample displays similar resonance features with peak values of tan δ_μ ~ 2.2 at 8 GHz and ~ 4.0 at 11.5 GHz, reflecting its partially restored magnetic ordering (Ms = 52.21 emu/g) and high magnetocrystalline anisotropy in large, well-faceted grains. Interestingly, the BSF-0.50 sample shows significantly suppressed magnetic loss (tan δ_μ < 2.3 throughout), consistent with its lowest saturation magnetization and disrupted superexchange coupling due to multiphase composition.

The complementary electromagnetic behavior observed across the three compositions reveals a critical trade-off between magnetic loss and dielectric loss contributions. BSF-0.25 exhibits strong magnetic loss but moderate dielectric loss, resulting in high permeability but potentially poor impedance matching (μ >> ε at certain frequencies). BSF-0.75 shows balanced but modest contributions from both mechanisms. Most significantly, BSF-0.50 demonstrates a dielectric-loss-dominated absorption profile, where the reduced magnetic loss (due to multiphase dilution and weakened superexchange) is more than compensated by exceptionally high dielectric loss from interfacial polarization. This compositional optimization achieves favorable impedance matching by balancing ε and μ values (as will be shown in Section 3.5), enabling efficient electromagnetic wave penetration and subsequent dissipation through combined Debye relaxation and residual magnetic resonance. These findings provide direct experimental evidence that optimal microwave absorption in Zn-substituted Ba–Sr hexaferrites is achieved not through maximizing magnetic loss (which would favor BSF-0.25), but through engineering a balanced

dual-loss mechanism with optimized impedance matching—a paradigm shift from conventional magnetization-centric design strategies.

3.5. Reflection loss performance

The microwave absorption performance was evaluated through frequency-dependent reflection loss (RL) measurements across the 4–12 GHz range, encompassing both C-band (4–8 GHz) and X-band (8–12 GHz) radar frequencies. Figure 5(a) presents the calculated RL curves based on the measured electromagnetic parameters (ε and μ from Fig. 4) using transmission line theory (Equations 1–2), while Table 2 summarizes the peak absorption performance metrics. All three compositions exhibit effective absorption (RL < − 10 dB, corresponding to > 90% absorption) across most of the tested frequency range, demonstrating the inherent potential of Zn-substituted Ba–Sr hexaferrites for broadband microwave attenuation applications. The BSF-0.50 sample achieves the most superior performance, with a minimum reflection loss of − 24.94 dB at 10.78 GHz (X-band), corresponding to 99.7% absorption efficiency. This peak performance is accompanied by an exceptionally broad effective absorption bandwidth, maintaining RL < − 10 dB across nearly the entire 4–12 GHz range. The BSF-0.25 sample displays the second-best performance with RL_{min} = −22.53 dB at 10.57 GHz (99.4% absorption), while BSF-0.75 exhibits the weakest absorption with RL_{min} = −20.14 dB at 10.76 GHz, despite achieving 99.8% absorption at its resonance frequency. Notably, all three compositions cluster their absorption peaks in the X-band region (~ 10.5–10.8 GHz), which is highly desirable for high-resolution radar and satellite communication applications.

The critical role of impedance matching in determining absorption efficiency is directly demonstrated in Fig. 5(b), which presents the frequency-dependent normalized input impedance ratio (Z_{in}/Z_0). Ideal impedance matching ($Z_{in}/Z_0 = 1$) minimizes surface reflection and enables maximum electromagnetic wave penetration into the absorber, where energy is subsequently dissipated through magnetic and dielectric loss mechanisms [22]. The BSF-0.50 sample exhibits the most favorable impedance matching behavior, with Z_{in}/Z_0 values fluctuating between 1.2 and 1.5 across most of the frequency range, remarkably close to the ideal unity condition. Although a sharp impedance spike to ~ 1.5 occurs at 8 GHz, likely arising from the interplay between natural ferromagnetic resonance (FMR) and Debye relaxation processes, the overall impedance stability in the X-band region (9–12 GHz) directly correlates with the superior RL performance observed at 10.78 GHz. In contrast, the BSF-0.25 and BSF-0.75 samples show more pronounced impedance deviations, with Z_{in}/Z_0 reaching values of 1.3–1.5, indicating less optimal matching conditions. This impedance behavior can be directly traced to the electromagnetic parameter balance (or imbalance) observed in Fig. 4: BSF-0.50 achieves favorable matching through its unique combination of moderate permittivity (ε' ~ 10–20) and moderate permeability (μ' ~ 5–15), which yield a balanced Z_{in}/Z_0 ratio according to Eq. (2), where $Z_{in} \propto \sqrt{(\mu_r/\varepsilon_r)}$. In contrast, BSF-0.25 exhibits high permeability (μ' ~ 20–60) relative to its permittivity (ε' ~ 10–20), resulting in $Z_{in}/Z_0 > 1$ and suboptimal matching despite its strong magnetic loss ($\tan \delta_M$ ~ 4 from

Fig. 4d). Conversely, BSF-0.75 shows high permittivity (ε' ~ 30–50) relative to its permeability (μ' ~ 10–20), also leading to impedance mismatch.

The systematic correlation between structural characteristics, electromagnetic properties, and absorption performance across the three compositions provides compelling experimental validation of the impedance-matching-dominated absorption paradigm. Most significantly, BSF-0.50 achieves the deepest reflection loss (− 24.94 dB) and broadest effective bandwidth despite exhibiting the lowest saturation magnetization (Ms = 37.29 emu/g, Table 2) and weakest magnetic loss (tan δ < 2.3, Fig. 4d) among the three samples. This counterintuitive result definitively demonstrates that maximum magnetic loss is not a sufficient—or even necessary—condition for optimal microwave absorption. Instead, the superior performance of BSF-0.50 originates from three synergistic factors: (1) optimized impedance matching (Z_i/Z_0 ≈ 1.2–1.4) arising from balanced ε and μ values, which maximizes wave penetration and minimizes surface reflection; (2) exceptionally high dielectric loss (tan δ ~ 3.8 at 9–11 GHz, Fig. 4c) driven by Maxwell-Wagner interfacial polarization at heterogeneous phase boundaries (M-type/Fe_3O_4/Fe_2O_3, XRD Fig. 1b) and dipolar relaxation in the coarse-grained microstructure (1.5–2.3 μm, SEM Fig. 2b); and (3) residual magnetic loss from natural ferromagnetic resonance, which, though weaker than BSF-0.25, contributes sufficient magnetic damping when combined with the dominant dielectric dissipation mechanism. Conversely, BSF-0.25, despite possessing the highest saturation magnetization (Ms = 57.95 emu/g) and strongest magnetic loss (tan δ ~ 3.9), achieves only moderate absorption (− 22.53 dB) due to impedance mismatch caused by excessive permeability relative to permittivity (μ >> ε), which increases surface reflection according to Eq. (1). These findings provide quantitative experimental evidence that challenges the traditional magnetization-dominant design paradigm in ferrite-based microwave absorbers and establish impedance matching optimization through compositional engineering as the decisive factor governing absorption efficiency. The demonstrated ability to tailor Zn substitution levels to optimize the magnetic–dielectric balance opens new pathways for rational design of high-performance X-band radar absorbing materials.

Table 2
The RL (reflection loss) value of the $Ba_{0.6}Sr_{0.4}Fe_{12-}ZnO_{19}$ (x = 0.25; 0.50 and 0.75) samples

Zn^{2+} doped (x)	Frequency (GHz)	RL (dB)	Microwave absorption (%)
0.25	10.57	−22.53	99.4
0.50	10.78	−24.94	99.7
0.75	10.76	-20.14	99.8

3.6. Microwave absorption mechanism

The microwave absorption behavior of Zn-substituted Ba–Sr hexaferrites is governed by the synergistic interplay between magnetic resonance, dielectric polarization, and impedance matching rather than by a

single dominant loss mechanism. Zn^{2+} substitution at Fe^{3+} sites (preferentially occupying tetrahedral $4f_1$ sites) leads to progressive weakening of Fe^{3+}–O^{2-}–Fe^{3+} superexchange interactions through two mechanisms: (i) direct dilution of magnetic exchange pathways by replacing magnetic Fe^{3+} (S = 5/2) with nonmagnetic Zn^{2+} (S = 0), and (ii) disruption of the rigid magnetoplumbite lattice structure, reducing the Fe–O–Fe bond angle from the optimal ~ 125° for strong superexchange coupling. This magnetic softening manifests as a reduction in saturation magnetization (Ms: 57.95 → 37.29 → 52.21 emu/g, Table 2) and magnetocrystalline anisotropy, which in turn shifts the natural ferromagnetic resonance (FMR) frequency according to $f_r = \gamma H_a$, where γ is the gyromagnic ratio and H_a is the anisotropy field. The FMR downshift enhances absorption in the C–X band frequency range (4–12 GHz), as evidenced by the multiple resonance peaks observed in magnetic loss tangent ($\tan \delta_\mu$) spectra (Fig. 4d) at 8 and 11 GHz, consistent with previous reports on substituted M-type hexaferrites [16–18].

Despite the systematic decrease in magnetic loss magnitude with increasing Zn content ($\tan \delta_\mu$ decreasing from ~ 3.9 to ~ 2.3, Fig. 4d), the dielectric loss component is simultaneously and dramatically enhanced ($\tan \delta_\varepsilon$ increasing from ~ 2.5 to ~ 3.8 at 9–11 GHz for BSF-0.50, Fig. 4c) through multiple complementary mechanisms. First, interfacial (Maxwell-Wagner) polarization arises at heterogeneous phase boundaries in the multiphase BSF-0.50 composition (M-type hexaferrite/Fe_3O_4/Fe_2O_3 interfaces, XRD Fig. 1b), where charge accumulation occurs due to conductivity and permittivity mismatches between phases. Second, dipolar polarization is induced by lattice defects, oxygen vacancies, and cation disorder resulting from Zn^{2+}/Fe^{3+} substitution, which create localized electric dipoles that respond to the alternating electromagnetic field. Third, grain boundary polarization is amplified by the coarse-grained microstructure (1.5–4.3 μm, SEM Fig. 2), which provides extensive interfacial area for charge carrier accumulation and subsequent Debye relaxation. Similar enhancement of dielectric loss induced by cation substitution and microstructural evolution has been widely reported in recent ferrite-based absorbers [17, 18]. Consequently, electromagnetic energy dissipation occurs through dual-loss pathways: (i) spin relaxation via natural ferromagnetic resonance and domain wall resonance in the magnetic phase, and (ii) polarization relaxation via Debye-type dielectric relaxation at phase boundaries and defect sites.

Most significantly, the BSF-0.50 composition exhibits the strongest microwave absorption performance (RL_{min} = −24.94 dB at 10.78 GHz, 99.7% absorption, Table 3) despite possessing the lowest saturation magnetization (Ms = 37.29 emu/g) and weakest magnetic loss ($\tan \delta_\mu$ < 2.3) among all samples. This counterintuitive result provides definitive experimental evidence that high magnetic loss alone is neither sufficient nor necessary for optimal microwave absorption. Instead, the superior performance originates from optimized impedance matching (Z_{in}/Z_0 ≈ 1.2–1.4, Fig. 5b), achieved through the balanced combination of moderate complex permittivity (ε' ~ 10–20, ε" ~ 5–15) and moderate complex permeability (μ' ~ 5–15, μ" ~ 5–10) in the X-band region. According to Eq. (2), the input impedance is proportional to $\sqrt{(\mu_r/\varepsilon_r)}$, such that balanced ε and μ values yield $Z_{in}/Z_0 \approx 1$, minimizing surface reflection and maximizing wave penetration into the absorber material. Once penetrated, electromagnetic energy is efficiently dissipated through the combined action of residual magnetic resonance (natural FMR) and

dominant dielectric relaxation (Maxwell-Wagner interfacial polarization), resulting in 99.7% absorption at the resonance frequency. In stark contrast, the BSF-0.25 composition, despite exhibiting the highest Ms (57.95 emu/g) and strongest magnetic loss (tan δ ~ 3.9), achieves only moderate absorption (RL_i = −22.53 dB) due to impedance mismatch arising from excessive permeability relative to permittivity (μ >> ε), which increases surface reflection and prevents effective wave entry. At higher Zn substitution (BSF-0.75), excessive grain growth (3.1–4.3 μm) and partial structural disorder lead to deteriorated impedance matching despite partial magnetization recovery, reducing absorption efficiency to RL_i = −20.14 dB.

The comparative performance analysis presented in Table 4 positions this work within the context of recent Zn-substituted hexaferrite absorbers. Previous studies on $Zn–SrFe_{12}O_{19}$ [15], $Co–Zn–BaFe_{12}O_{19}$ [13], and Ca–Co substituted $BaFe_{12}O_{19}$ [18] systems report reflection loss values ranging from − 21.5 to − 23.0 dB across broad frequency ranges (1–18 GHz or 2–18 GHz) with thicknesses of 2.0–2.5 mm. Notably, all these previous works attribute their absorption performance primarily to "magnetic loss dominant" or "magnetic resonance" mechanisms, emphasizing the role of high saturation magnetization and strong ferromagnetic coupling. In contrast, the present $Ba_{0.6}Sr_{0.4}Fe_{12-}Zn O_{19}$ system achieves a superior reflection loss of − 24.94 dB within a targeted X-band frequency range (4–12 GHz) at a comparable thickness (2.0 mm), while the absorption mechanism is fundamentally different: "magnetic–dielectric synergy & impedance matching". This mechanistic distinction represents a paradigm shift from conventional magnetization-centric design strategies. Rather than maximizing magnetic loss through high Ms and strong superexchange coupling, this work demonstrates that optimal absorption is achieved by engineering a balanced dual-loss system where moderate magnetic loss and high dielectric loss are synergistically combined with optimized impedance matching (Z_i/Z_0 ≈ 1). The targeted frequency range (4–12 GHz) covers critical C–X band radar and satellite communication frequencies, making this approach particularly relevant for practical applications in high-resolution radar systems and stealth technology. These results provide quantitative experimental validation that impedance matching optimization through compositional and microstructural engineering—rather than magnetic loss maximization—governs microwave absorption efficiency in Zn-substituted Ba–Sr M-type hexaferrites, establishing new design principles for next-generation ferrite-based absorbers [16–18, 22].

Table 3
Comparison of microwave absorption performance of Zn-substituted hexaferrites reported in the literature

Material system	Frequency range (GHz)	RLmin (dB)	Thickness (mm)	Key mechanism	Ref.
Zn–$SrFe_{12}O_{19}$	2–18	−21.5	2.0	Magnetic loss dominant	[15]
Co–Zn–$BaFe_{12}O_{19}$	1–18	−23.0	2.5	Magnetic resonance	[13]
Ca–Co substituted $BaFe_{12}O_{19}$	1–18	−22.8	2.0	Magnetic resonance	[18]
$Ba_{0.6}Sr_{0.4}Fe_{12-}$ZnO_{19} (this work)	4–12	−24.94	2.0*	Magnetic–dielectric synergy & impedance matching	This work

4. Conclusion

This study systematically investigated the effects of Zn substitution on the structural, magnetic, and electromagnetic properties of $Ba_{0.6}Sr_{0.4}Fe_{12-}$ZnO_{19} (x = 0.25, 0.50, 0.75) M-type hexaferrites synthesized via solid-state reaction, with emphasis on elucidating the mechanisms governing microwave absorption performance in the technologically important C–X band (4–12 GHz). X-ray diffraction analysis revealed that increasing Zn content induced multiphase formation (x = 0.50) and progressive lattice expansion, while SEM characterization demonstrated systematic grain coarsening from 200–300 nm to 3.1–4.3 μm. Magnetic measurements showed non-monotonic magnetization behavior, with saturation magnetization decreasing from 57.95 emu/g (x = 0.25) to 37.29 emu/g (x = 0.50) before partially recovering to 52.21 emu/g (x = 0.75), reflecting the competing effects of Zn-induced superexchange weakening and microstructural evolution.

Most significantly, the intermediate composition (x = 0.50) achieved superior microwave absorption performance with a minimum reflection loss of − 24.94 dB at 10.78 GHz (99.7% absorption efficiency), despite exhibiting the lowest saturation magnetization and weakest magnetic loss among all samples. This counterintuitive result provides definitive experimental evidence that optimal microwave absorption is governed by impedance matching optimization (Z_i/Z_0 ≈ 1) through balanced magnetic–dielectric synergy, rather than by magnetic loss magnitude alone. The enhanced performance originates from synergistic contributions of Maxwell-Wagner interfacial polarization at heterogeneous phase boundaries, residual ferromagnetic resonance, and optimized impedance matching enabled by compositional engineering. These findings challenge the conventional magnetization-dominant design paradigm and establish impedance-matching-dominated principles for rational design of high-performance ferrite-based microwave absorbers for X-band radar, satellite communication, and stealth technology applications.

Declarations

Acknowledgements

Universitas Pelita Harapan funded this research with P-004-RInG-FIP/VII/2024 contract numbers.

Author contributions

Maya Puspitasari Izaak: Conceptualization, Methodology, Investigation, Formal analysis, Data curation, Writing – original draft. **Henni Sitompul**: Investigation, Formal analysis, Data curation, Validation. **Yana Taryana**: Methodology, Investigation, Resources, Validation. **Nanang Sudrajat**: Investigation, Data curation, Formal analysis. **Jan Setiawan**: Methodology, Investigation, Formal analysis, Data curation, Writing – original draft. **Yunasfi Yunasfi**: Formal analysis, Validation, Writing – review & editing, Supervision. **Mashadi Mashadi**: Methodology, Investigation, Data curation, Writing – original draft, Project administration. **Didin S. Winatapura**: Investigation, Formal analysis, Conceptualization, Resources. **Wisnu Ari Adi**: Validation, Resources, Writing – review & editing, Supervision. **Tesalonika Siregar**: Visualization, Investigation, Data curation, Software. **Yohanes Edi Gunanto**: Conceptualization, Formal analysis, Resources, Writing – review & editing, Supervision, Funding acquisition. **Dianta Ginting**: Conceptualization, Methodology, Formal analysis, Writing – review & editing, Supervision, Project administration.

Conflicts of interest or competing interests

The authors affirm that they have no known competing financial interests or personal relationships that could have appeared to influence the work presented in this manuscript

Data and code availability

Data will be made available on request.

Supplementary information

There is no supplementary information accompanying this manuscript

Ethical approval

Not Applicable.

References

1. Z. Cui *et al.*, "Recent advances in carbon composite films for high-performance, multifunctional and intelligent electromagnetic interference shielding and electromagnetic wave absorption," *Carbon N. Y.*, vol. 230, no. 37, p. 119627, 2024, doi: 10.1016/j.carbon.2024.119627.

2. A. Massa *et al.*, "Designing Smart Electromagnetic Environments for Next-Generation Wireless Communications," *Telecom*, vol. 2, no. 2, pp. 213–221, 2021, doi: 10.3390/telecom2020014.
3. K. Chen *et al.*, "Lightweight but ultrahigh-strength functionally integrated absorbers: Highly effective electromagnetic wave absorption and infrared stealth," *Chem. Eng. J.*, vol. 507, no. November 2024, p. 160646, 2025, doi: 10.1016/j.cej.2025.160646.
4. Q. Li *et al.*, "Engineering strategies in low-dimensional microwave absorbers: Fundamentals, progress, and outlook," *Mater. Sci. Eng. R Reports*, vol. 159, no. December 2023, 2024, doi: 10.1016/j.mser.2024.100795.
5. J. Li *et al.*, "Recent progress in two-dimensional materials for microwave absorption applications," *Chem. Eng. J.*, vol. 425, no. August, p. 131558, 2021, doi: 10.1016/j.cej.2021.131558.
6. K. Singha *et al.*, "A review of Z-type hexaferrite based magnetic nanomaterials: Structure, synthesis, properties, and potential applications," *Prog. Solid State Chem.*, vol. 70, no. April, p. 100404, 2023, doi: 10.1016/j.progsolidstchem.2023.100404.
7. I. Mohammed *et al.*, "Review on Y-type hexaferrite: Synthesis, characterization and properties," *Appl. Surf. Sci. Adv.*, vol. 16, no. November 2022, p. 100416, 2023, doi: 10.1016/j.apsadv.2023.100416.
8. A. Lobo-Guerrero, V. E. Salazar-Muñoz, R. H. A. Del Toro, and E. E. Hernández-Vázquez, "M-type hexaferrites: A review of the impact of rare earth substitution on magnetic properties," *J. Magn. Magn. Mater.*, vol. 627, no. April, 2025, doi: 10.1016/j.jmmm.2025.173132.
9. M. Zahid, S. Siddique, R. Anum, M. F. Shakir, Y. Nawab, and Z. A. Rehan, "M-Type Barium Hexaferrite-Based Nanocomposites for EMI Shielding Application: a Review," *J. Supercond. Nov. Magn.*, vol. 34, no. 4, pp. 1019–1045, 2021, doi: 10.1007/s10948-021-05859-1.
10. Y. Slimani *et al.*, "Structural, magnetic, and microwave features of Sc3+ ions substituted Sr0.5Ba0.5Fe12O19 nanohexaferrites," *J. Alloys Compd.*, vol. 976, no. October 2023, p. 173138, 2024, doi: 10.1016/j.jallcom.2023.173138.
11. Y. Marouani *et al.*, "Electrical conductivity and dielectric properties of Sr doped M-type barium hexaferrite BaFe12O19," *RSC Adv.*, vol. 11, no. 3, pp. 1531–1542, 2021, doi: 10.1039/d0ra09465j.
12. M. Kumar Manglam *et al.*, "Study of dipole polarization in Zn doped barium hexaferrite," *Mater. Today Proc.*, vol. 66, pp. 1862–1864, 2022, doi: 10.1016/j.matpr.2022.05.290.
13. F. Z. Mohammad, F. Huma, and K. Ali, "Magnetic and microwave absorption properties of Co2+ and Zn2+ co-doped barium hexaferrite nanoparticles," *J. Mater. Sci. Mater. Electron.*, vol. 34, no. 12, pp. 1–12, 2023, doi: 10.1007/s10854-023-10377-y.
14. A. Tadjarodi, R. Rahimi, M. Imani, H. Kerdari, and M. Rabbani, "Synthesis, characterization and microwave absorbing properties of the novel ferrite nanocomposites," *J. Alloys Compd.*, vol. 542, pp. 43–50, 2012, doi: 10.1016/j.jallcom.2012.07.049.
15. N. L. Tuyen *et al.*, "Excellent microwave absorption performance of zinc-doped SrFe12O19 hexaferrite and detailed loss mechanism," *J. Sci. Adv. Mater. Devices*, vol. 9, no. 4, 2024, doi: 10.1016/j.jsamd.2024.100796.

16. P.D. Mhase, P. D., Advances in M-type hexaferrites: A review tailoring structural, magnetic, and microwave absorption properties for emerging technologies. *Coordination Chemistry Reviews*, *541*, 216825, 2025; https://doi.org/10.1016/j.ccr.2024.216825
17. W. Li, and P. Singh, P., Microwave absorption mechanisms in substituted barium ferrites: A comprehensive review. *Journal of Magnetism and Magnetic Materials*, *565*, 170288, 2023; https://doi.org/10.1016/j.jmmm.2022.170288
18. D. Wang, M. Wang, F. Liu, Y. Cui, Q. Zhao, H. Sun, H. Jin, and M. Cao, Microwave absorption and magnetic properties of M-type hexagonal ferrite $Ba_{0.95}Ca_{0.05}Fe_{12-}$□$Co$□$O_{19}$ ($0 \le x \le 0.4$) at 1–18 GHz. *Materials*, *17*(21), 5327, 2024; https://doi.org/10.3390/ma17215327
19. S. H. Kim, S. Y. Lee, Y. Zhang, S. J. Park, and J. Gu, "Carbon-Based Radar Absorbing Materials toward Stealth Technologies," *Adv. Sci.*, vol. 10, no. 32, pp. 1–22, 2023, doi: 10.1002/advs.202303104.
20. M. Abdel-Megid, M. E. Eissa, A. T. Mosleh, N. A.M. Ragab, H. Y. Zahran, I. S. Yahia, E. A. Kamoun, M.H. Ghozza, Magnetic, electrical, and dielectric properties of microwave-assisted synthesis of $Bi_{0.6}Sr_{0.4}FeO_3$ nanoparticles for wastewater treatments: Electro-degradation of Rhodamine B dye, Ceramics International, Volume 51, Issue 23, Part B, 2025, 39677-39687, https://doi.org/10.1016/j.ceramint.2025.06.203.
21. Y. Yunasfi, J. Setiawan, M. Mashadi et al. Cationic distribution analysis of lanthanum doped Cobalt nickel titanate as microwave absorbing material and its correlation with weak ferromagnetic behavior. emergent mater. (2025). https://doi.org/10.1007/s42247-025-01166-w
22. X. Chen, Emerging broadband shielding materials: From synthesis to performance optimization. *Materials Today Communications*, *42*, 105123, 2025; https://doi.org/10.1016/j.mtcomm.2024.105123

Figures

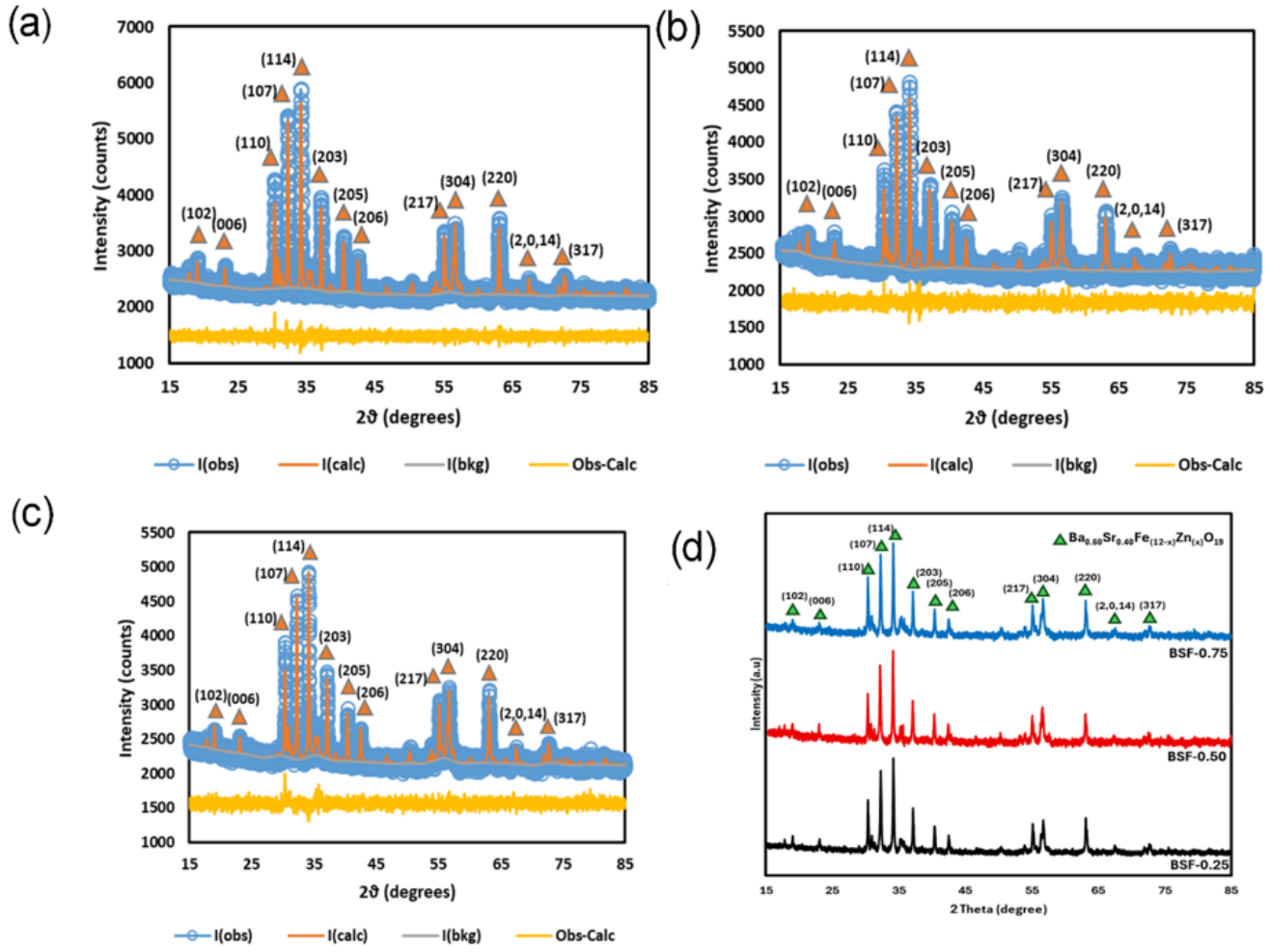


Figure 1

Rietveld-refined XRD patterns of $Ba_{0.6}Sr_{0.4}Fe_{12-}$ZnO_{19} hexaferrites: (a) BSF-0.25, (b) BSF-0.50, (c) BSF-0.75, and (d) comparative overlay. Peaks are indexed to M-type hexagonal structure (space group $P6_3/mmc$, JCPDS 43-0002). Secondary phases (Fe_3O_4, Fe_2O_3) are observed in BSF-0.50.3.2. Microstructure and grain evolution

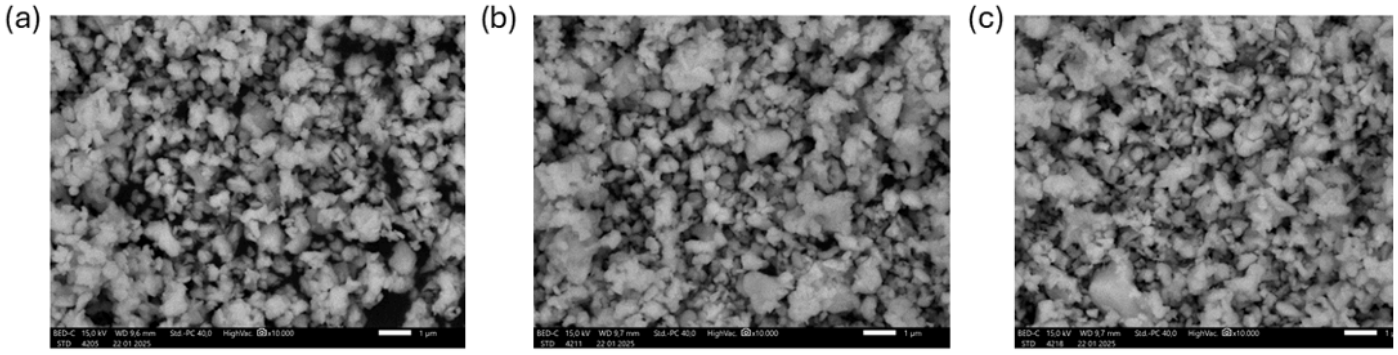


Figure 2

SEM micrographs of $Ba_{0.6}Sr_{0.4}Fe_{12-}ZnO_{19}$ hexaferrites at 10,000× magnification: (a) BSF-0.25 (grain size: 200–300 nm), (b) BSF-0.50 (1.5–2.3 μm), and (c) BSF-0.75 (3.1–4.3 μm). Progressive grain coarsening with increasing Zn content is evident.

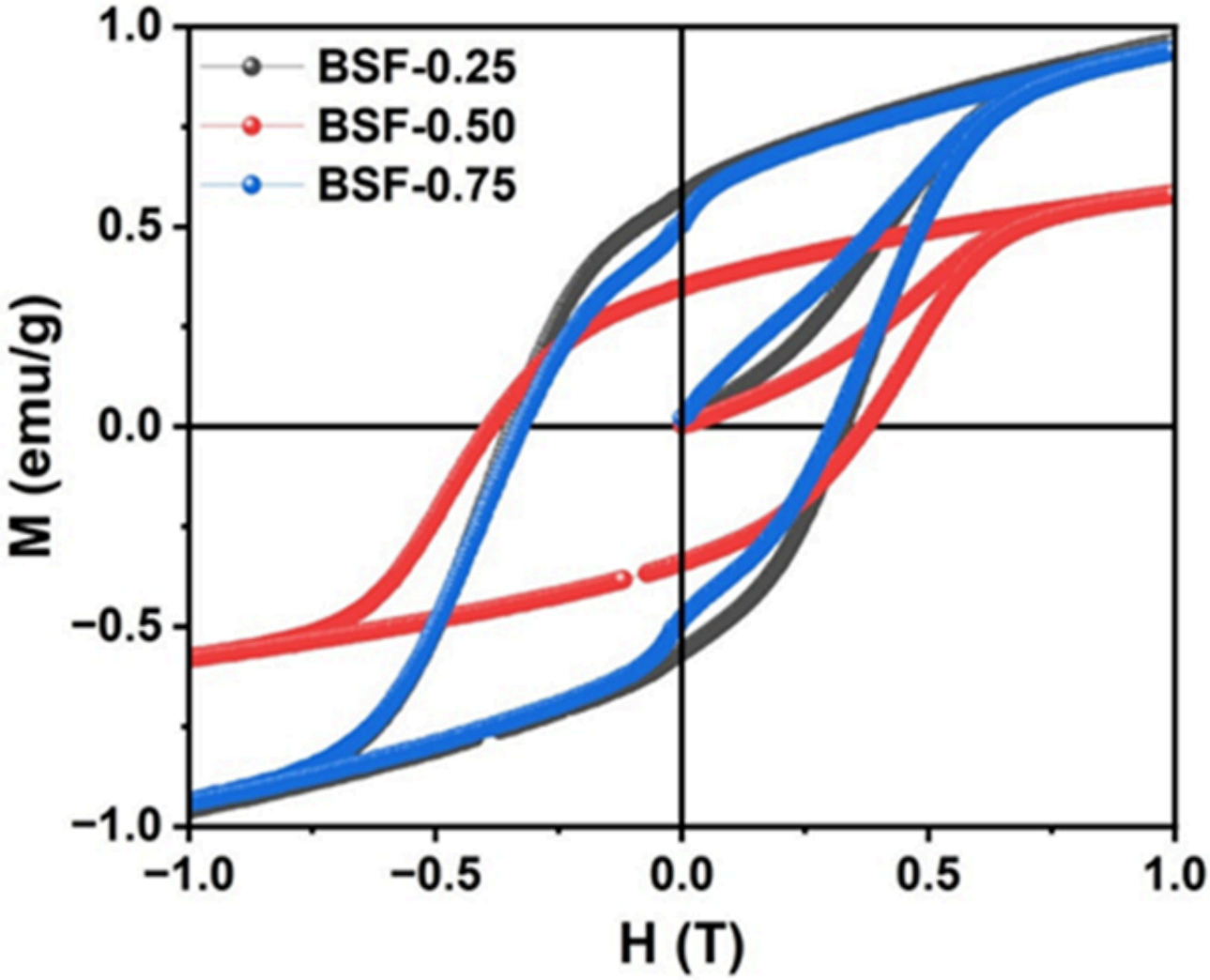


Figure 3

Magnetic hysteresis loops of $Ba_{0.6}Sr_{0.4}Fe_{12-}ZnO_{19}$ hexaferrites measured at 300 K under ±1 T applied field. BSF-0.25 exhibits the highest saturation magnetization and squarest loop, while BSF-0.50 shows significant magnetic softening due to multiphase composition. BSF-0.75 displays partial magnetic recovery with the lowest coercivity.

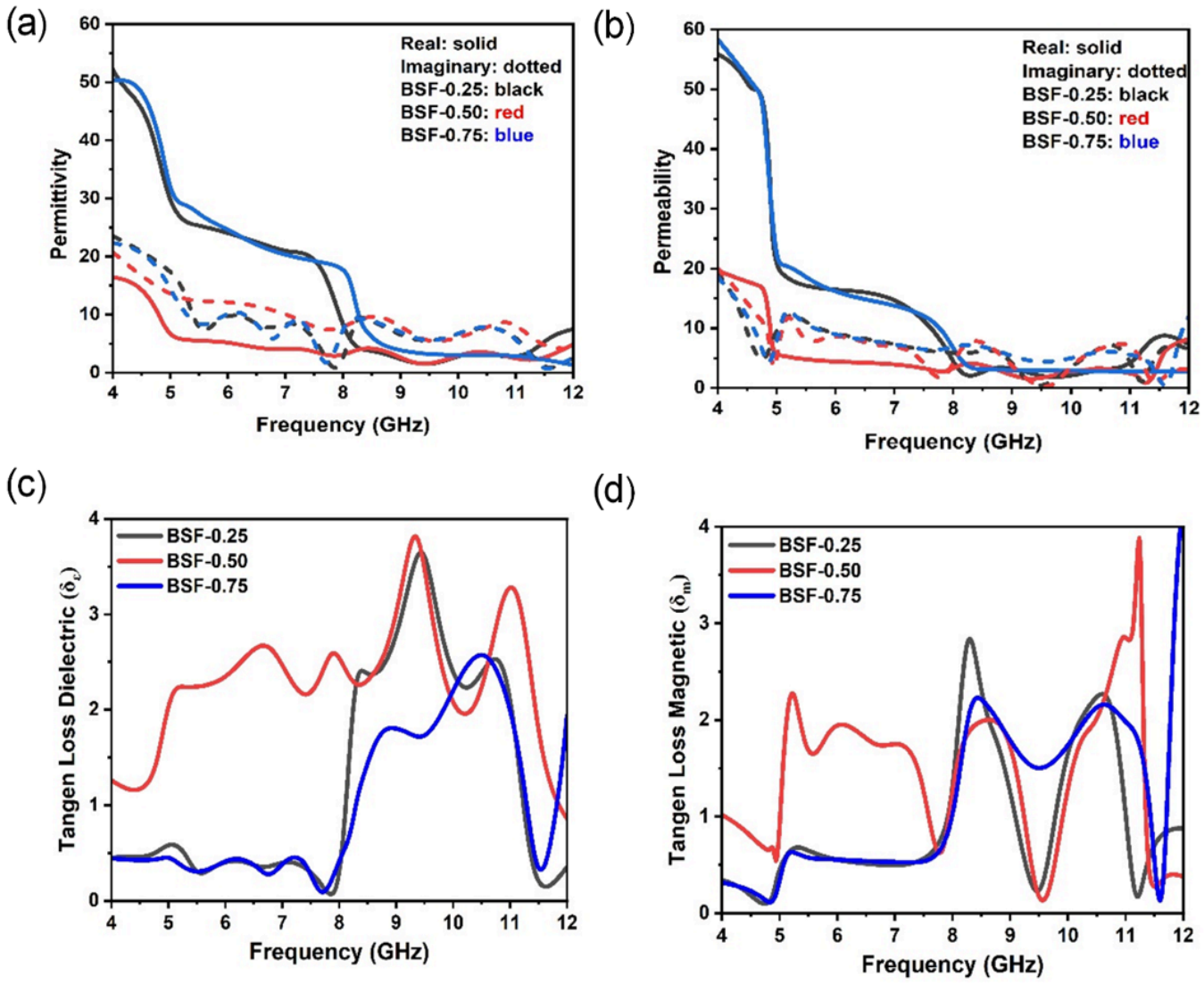


Figure 4

Frequency-dependent electromagnetic parameters of $Ba_{0.6}Sr_{0.4}Fe_{12-}$ZnO_{19} hexaferrites (4–12 GHz): (a) Complex permittivity (ε' solid, ε" dotted), (b) Complex permeability (μ' solid, μ" dotted), (c) Dielectric loss tangent (tan δ), and (d) Magnetic loss tangent (tan δ). BSF-0.50 exhibits dominant dielectric loss with peaks at 9–11 GHz, while BSF-0.25 shows strong magnetic resonance at 8 and 11 GHz. Complementary loss mechanisms enable impedance optimization.

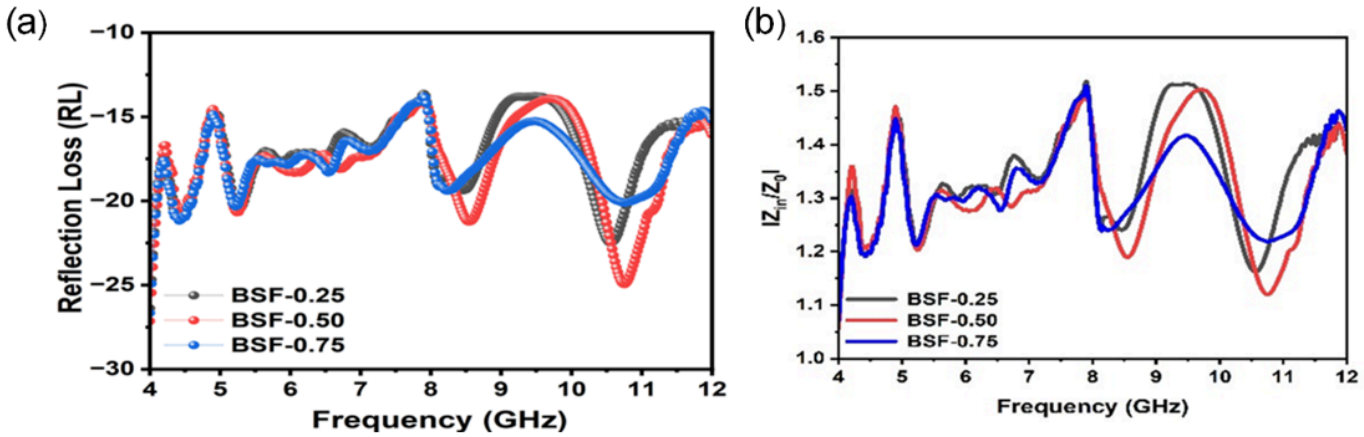


Figure 5

(a) Frequency-dependent reflection loss (RL) curves calculated from measured electromagnetic parameters showing BSF-0.50 achieves minimum RL of −24.94 dB at 10.78 GHz with broadest effective bandwidth (RL < −10 dB across 4–12 GHz). (b) Normalized input impedance ratio (Z□□/Z_0) demonstrating BSF-0.50's superior impedance matching (Z□□/Z_0 ≈ 1.2–1.4) correlates with optimal absorption performance, validating impedance-matching-dominated mechanism over magnetic-loss-dominated paradigm.